Brownian dynamics of polymer migration in combined pressure-driven and electrophoretic flows

Petr Hotmar*, Ravi Chella†
Department of Chemical and Biomedical Engineering,
Florida State University

Abstract

We examine DNA electrophoresis under pressure-driven flow in a microchannel using Brownian Dynamics. In addition to hydrodynamic interactions due to non-electric forces, we also include electrically-induced hydrodynamic interactions, which arise due to velocity disturbances generated by localized bead charges and their counter-ion clouds. All modeled bulk interactions are supplemented with the appropriate wall corrections, thus providing a uniformly valid solution for small Debye lengths. We analyze cross-stream migration patterns in light of competition among different types of hydrodynamic interactions and show the Peclet number dependence of electrophoretic mobility and radius-of-gyration tensor in moderate flows.

Keywords: *Brownian dynamics, DNA electrophoresis, Poiseuille flow, rectangular channel, hydrodynamic interactions, cross-stream migration*

1 Introduction

The dynamics of confined polymer solutions is of practical interest most notably to biomolecular manipulation in microfluidic devices [2, 3, 25]. Indirectly, polymer solutions serve as a prototypical model for other complex and multiphase fluids, including colloidal suspensions. A significant component of this dynamics, with potential use in separation applications, is cross-stream migration of a polyelectrolyte such as DNA. The migration is a manifestation of hydrodynamic interactions among the individual sections of the chain, mediated by the fluid and, also significantly, by the walls.

*email: ph06@fsu.edu
†email: rchella@fsu.edu

For DNA in uniform shear flow, cross-stream migration away from the walls has been observed both experimentally and in simulations [12] for strongly confined systems (with characteristic channel dimension H on the order of the polymer radius of gyration R_g). For DNA in an electrolyte under an imposed electric field, hydrodynamic interactions are attenuated by the counterion clouds which surround the charged macroions, but the screening is not exponential; a residual flow from the quadrupole moment of the charge density remains [16, 1]. While its long-range part decays faster than the regular point-force disturbance in an uncharged solvent (regular Stokeslet), the decay is still algebraic and thus non-negligible except for extremely small Debye lengths (or, equivalently, large salt concentrations). In fact, recent research [27, 14] indicates non-trivial migration behavior (both towards, and away from, the walls) in weak confinements ($H \approx 100R_g$) when the flow is coupled with an external electric field. The electrically-induced hydrodynamic interactions have been shown to be the primary source of this migration.

To provide a treatment of the hydrodynamic interactions more complete than that commonly adopted [6, 14], we include both short-ranged and long-ranged parts of the point-force solution (electrophoretic Stokeslet) of the Stokes flow in an electrolyte. More importantly, rather than assuming that the wall correction to the electrophoretic Stokeslet can be either neglected [6] (correct in the limit of zero Debye length) or approximated by the wall correction due to the regular Stokeslet [14] (correct for large Debye lengths), we include it directly.

The layout is as follows. In Sec. 2 we give the theoretical background on the mobility tensors associated with the nonhydrodynamic and electric forces acting on both the polymer chain and the solvent, and discuss how these tensors are used in Brownian dynamics. In Sec. 3 we describe the imposed flow and external field and characterize their strengths in terms of Weissenberg and Peclet numbers, respectively. Sec. 4 discusses the issues and results related to the divergence of the diffusion tensor, an important term in the Brownian dynamics equation. Sec. 5 focuses on the cross-stream migration. First it shows, in the context of kinetic theory, how the individual contributions to the migration arise due to different types of hydrodynamic interactions. It then discusses the consequences of the competition between these interactions, before presenting our migration results of Brownian dynamics simulations.

2 Theoretical background

As in our previous work [10], we use a bead-spring model for a λ-phage DNA as a prototypical polyelectrolyte with the following set of coarse-grained parameters: contour length $L = 21\,\mu$m, number of springs $N_s = 10$, Kuhn length $b_k = 0.1\,\mu$m and bead radius $a = 0.077\,\mu$m. These parameters were determined by Jendrejack [11] from experimental data for stained λ-phage DNA. The solvent is an aqueous binary electrolyte with dynamic viscosity $\eta = 43.3$ cP, absolute temperature $T = 298$ K and varying ionic strength (with Debye lengths $\lambda_D = 10, 10^2$ and 10^3 nm for average and low salt concentrations).

In an unconfined pure dielectric (no free charges), the velocity perturbation $\boldsymbol{v}'_h$ is only due to the hydrodynamic force $\boldsymbol{F}^h$; thus $\boldsymbol{v}'_h = -\boldsymbol{\Omega}^{OB} \cdot \boldsymbol{F}^h$, where $\boldsymbol{\Omega}^{OB}$ is the Green's function of the Stokes equation (Oseen-Burgers Stokeslet). For N beads, the force balance between the Brownian $\boldsymbol{F}^b$, spring $\boldsymbol{F}^s$, electric $\boldsymbol{F}^e$ and hydrodynamic forces $\boldsymbol{F}^h = -\zeta\left[\dot{\boldsymbol{r}} - (\boldsymbol{u} + \boldsymbol{v}'_h)\right]$, yields the velocity of the i-th bead [15],

$$\dot{\boldsymbol{r}}_i = \boldsymbol{u}(\boldsymbol{r}_i) + \sum_{j=1}^{N} \boldsymbol{\mu}_{ij} \cdot \left(\boldsymbol{F}^b_j + \boldsymbol{F}^s_j + \boldsymbol{F}^e_j\right), \tag{1}$$

where $\zeta = \mu^{-1}$ is the Stokes friction coefficient $6\pi\eta a$, $\boldsymbol{u}$ is the imposed velocity field and the HI mobility tensor $\boldsymbol{\mu}_{ij} = \delta_{ij}\mu\boldsymbol{I} + (1-\delta_{ij})\boldsymbol{\Omega}^{OB}_{ij}$, with δ_{ij} the Kronecker delta and $\boldsymbol{I}$ the identity dyad.

In an unconfined electrolyte, additional velocity perturbations arise due to the counter-ion cloud (CIC) which surrounds the backbone charges, $\boldsymbol{v}'_c = [\delta_{ij}\mu_c\boldsymbol{I} + (1-\delta_{ij})\boldsymbol{\Omega}^c_{ij}] \cdot \boldsymbol{F}^e$, where μ_c is the contribution to the mobility of an isolated bead due to CIC. The force balance with $\boldsymbol{F}^h = -\zeta\left[\dot{\boldsymbol{r}} - (\boldsymbol{u} + \boldsymbol{v}'_h + \boldsymbol{v}'_c)\right]$ yields

$$\dot{\boldsymbol{r}}_i = \boldsymbol{u}(\boldsymbol{r}_i) + \sum_{j=1}^{N} \boldsymbol{\mu}_{ij} \cdot \left(\boldsymbol{F}^b_j + \boldsymbol{F}^s_j\right) + \sum_{j=1}^{N} \boldsymbol{\mu}^e_{ij} \cdot \boldsymbol{F}^e_j, \tag{2}$$

where the electric HI mobility tensor $\boldsymbol{\mu}^e_{ij} = \delta_{ij}\mu_0\boldsymbol{I} + (1-\delta_{ij})\boldsymbol{\Omega}^{LA}_{ij}$ and the electrophoretic Stokeslet $\boldsymbol{\Omega}^{LA} \equiv \boldsymbol{\Omega}^{OB} + \boldsymbol{\Omega}^c$, which is equivalent to the Long-Ajdari form [16] . This splitting illustrates the additional contribution of $\boldsymbol{\Omega}^c$, which arises due to the CIC electric force density $\boldsymbol{f}_c(\boldsymbol{r}) = -\boldsymbol{F}^e\kappa^2\exp(-\kappa r)/(4\pi r)$, as induced around a point charge Q by electric force $\boldsymbol{F}^e = Q\boldsymbol{E}$ in the Debye-Hückel electrolyte with Debye length $\lambda_D \equiv$

κ^{-1}. The singularly-forced Stokes equation with point-charge force density $\boldsymbol{f}_{OB} = \boldsymbol{F}^e\delta(\boldsymbol{r})$ and CIC force density $\boldsymbol{f}_c$ can be solved by Fourier transform to give [16]

$$\boldsymbol{\Omega}^{OB,c} = \frac{1}{8\pi\eta r}\left[a\boldsymbol{I} + b\frac{\boldsymbol{r}\boldsymbol{r}}{r^2}\right], \tag{3}$$

where

$$a(s) = \begin{cases} 1 & \text{for } \boldsymbol{\Omega}^{OB}, \\ \frac{-\mathrm{e}^{-s}}{s^2}\left[\mathrm{e}^s(s^2+2) - 2(s^2+s+1)\right] & \text{for } \boldsymbol{\Omega}^{c}; \end{cases} \tag{4}$$

$$b(s) = \begin{cases} 1 & \text{for } \boldsymbol{\Omega}^{OB}, \\ \frac{-\mathrm{e}^{-s}}{s^2}\left[\mathrm{e}^s(s^2-6) + 2(s^2+3s+3)\right] & \text{for } \boldsymbol{\Omega}^{c}, \end{cases} \tag{5}$$

$\delta(\boldsymbol{r})$ is the Dirac delta function, $s = \kappa r$ and $r = |\boldsymbol{r}|$. To recover the correct electrophoretic mobility of an isolated bead μ_0, we obtain $\mu_c = \mu_0 - \mu$. The specific choice of μ_0 is discussed later in the text.

In confinement, the HI mobility tensors must include the wall corrections $\boldsymbol{\Omega}^W$ and $\boldsymbol{\Omega}^{W,e}$ corresponding to the regular and electrophoretic Stokeslets, respectively, which can be computed by solving the Stokes equation with an appropriately chosen image system. We then obtain the dyadic components of the 4th order mobility tensors $\boldsymbol{\mu}$ and $\boldsymbol{\mu}^e$ as

$$\boldsymbol{\mu}_{ij} = \delta_{ij}\mu\boldsymbol{I} + \boldsymbol{\Omega}_{ij}, \quad \text{where } \boldsymbol{\Omega}_{ij} \equiv (1-\delta_{ij})\boldsymbol{\Omega}^{OB}_{ij} + \boldsymbol{\Omega}^{W}_{ij}; \tag{6}$$

$$\boldsymbol{\mu}^e_{ij} = \delta_{ij}\mu_0\boldsymbol{I} + \boldsymbol{\Omega}^e_{ij}, \quad \text{where } \boldsymbol{\Omega}^e_{ij} \equiv (1-\delta_{ij})\boldsymbol{\Omega}^{LA}_{ij} + \boldsymbol{\Omega}^{W,e}_{ij}. \tag{7}$$

To ensure positive-semidefiniteness of $\boldsymbol{\mu}$ in our BD simulations, we use the Rotne-Prager-Yamakawa (RPY) regularization of the Oseen-Burgers free-space tensor; in what follows, $\boldsymbol{\Omega}^{OB}$ is thus to be interpreted as such.

To proceed with further developments, the form of Brownian force must be specified. One option is $\boldsymbol{F}^b dt = \sqrt{2k_bT\zeta}d\boldsymbol{w}$, where k_b is Boltzmann constant, T the absolute temperature, $\boldsymbol{w}$ is the Wiener process and the prefactor follows from the fluctuation-dissipation theorem relating the second moment of the velocity to its equilibrium value. This representation necessitates solving a coupled system of Langevin equation for the polymer and Landau-Lifshitz Navier-Stokes equation (LLNSE) for the solvent, also known as CLEPS framework [21], and was explored in our previous work on voltage-driven polymer translocation [10]. Another option is to use the equation of motion, Eq. 2, to write the Fokker-Planck equation governing the configurational distribution function $\psi(t, \boldsymbol{r})$ and, assuming equilibration in momentum space [4], adopt the smoothed Brownian force

$\boldsymbol{F}^b = -k_bT\frac{\partial \ln \psi}{\partial \boldsymbol{r}}$. This formulation, which is particularly useful in the kinetic theory of dilute polymer solutions, was employed in our previous work on confined FENE dumbells under electric field and pressure-driven flow [9]. The Fokker-Planck equation can be recast into the stochastic differential equation used in Brownian dynamics, where existence and uniqueness of the solution is guaranteed if the drift and diffusion terms satisfy Lipschitz and linear growth conditions [20]. We then obtain

$$d\boldsymbol{r} = \left[\boldsymbol{u} + \frac{1}{k_bT}\boldsymbol{D}\cdot\boldsymbol{F} + \frac{\partial}{\partial \boldsymbol{r}}\cdot\boldsymbol{D} + \boldsymbol{\mu}^e\cdot\boldsymbol{F}^e\right]dt + \sqrt{2}\boldsymbol{B}\cdot d\boldsymbol{w}, \tag{8}$$

$$\boldsymbol{D} = \boldsymbol{B}\cdot\boldsymbol{B}^T. \tag{9}$$

where $\boldsymbol{D}$ and $\boldsymbol{B}$ are the diffusion and stochastic tensors discussed below, $\boldsymbol{r}$ is the $3N$ vector of all bead positions, and $\boldsymbol{F}$ the $3N_b$ vector of all non-hydrodynamic forces, with N the number of beads. Aside from the Marko-Siggia spring force, these forces include a soft excluded-volume force and steric wall repulsion and are discussed in detail in [10]. The $\nabla\cdot\boldsymbol{D}$ term in Eq. 8 is the consequence of applying Îto calculus to the diffusion term in the Fokker-Planck equation, or, equivalently, the result of including a noise term in LLNSE. The matrix $\boldsymbol{D}$ is effectively a covariance matrix, therefore symmetric and positive-semidefinite. The Wiener increments are Gaussian distributed with zero mean and variance dt.

The regular HIs due to the Oseen disturbance field are included in the 4th order $3N\times 3N$ diffusion tensor $\boldsymbol{D}$ with component dyads $\boldsymbol{D}_{ij} = k_bT\boldsymbol{\mu}_{ij}$ (analogously, we can define the electrophoretic diffusion tensor $\boldsymbol{D}^e_{ij} = k_bT\boldsymbol{\mu}^e_{ij}$). The decomposition of the HI tensor $\boldsymbol{\Omega}$ into the free-space contribution and wall correction, Eq. 6, circumvents the need to solve a non-homogeneous Stokes equation with Dirac delta forcing on the right hand side, a computationally challenging task. Instead, having the free-space Green's function for the singularly-forced Stokes equation available in analytical form, the wall correction $\boldsymbol{u}^W$ can be obtained by numerically solving the homogeneous Stokes equation with non-homogeneous wall boundary conditions:

$$-\nabla p + \eta\Delta\boldsymbol{u}^W = 0,\ \ \nabla\cdot\boldsymbol{u}^W = 0, \tag{10}$$

$$\frac{\partial}{\partial n}\boldsymbol{u}^W = 0,\ p = 0 \qquad \text{for } \mathbf{x}\in\Gamma_I\cup\Gamma_O,$$

$$\boldsymbol{u}^W = -\boldsymbol{u}^{OB},\ \frac{\partial}{\partial n}p = -\eta\mathbf{n}\cdot(\nabla\times\nabla\times\boldsymbol{u}^W) \quad \text{for } \mathbf{x}\in\Gamma_W, \tag{11}$$

where $\mathbf{n}$ represents a unit normal to the surface and Γ_W, Γ_I and Γ_O are boundary segments corresponding to the walls, inlet and outlet of the domain, respectively. The wall correction $\boldsymbol{u}^W(\boldsymbol{x}, \boldsymbol{x_j})$ to the disturbance velocity due to a point force at $\boldsymbol{x_j}$ ensures no-slip at the walls and generates the corresponding correction tensor, since $\boldsymbol{u}^W(\boldsymbol{x}, \boldsymbol{x_j}) = \boldsymbol{\Omega}^W(\boldsymbol{x}, \boldsymbol{x_j}) \cdot \boldsymbol{f}(\boldsymbol{x}_j)$. The above system of equations is solved in a rectangular channel using a finite difference method with pressure damping, as outlined in our previous work [10]. We choose a coordinate system where the axial channel direction is along the x-axis and the walls are located at $y = 0, H$ and $z = 0, W$, where for simplicity we assume $H = W$ (this assumption is nonessential and can be removed without difficulty). At the inlet and outlet ($\Gamma_I \cup \Gamma_O$), we assume equalized pressures and zero shear stress as the open boundary condition for velocity. At the walls (Γ_W), we enforce no slip velocity ($\boldsymbol{v}^W + \boldsymbol{v}^{OB} = 0$) and the curl-curl boundary condition for pressure [22], which is a convenient reformulation of applying the normal component of the momentum equation at the boundary along with $\frac{\partial}{\partial n}(\nabla \cdot \boldsymbol{v}^W) = 0$.

The electrically-induced HIs will be strongly dependent on the choice of the single particle mobility μ_0. Each bead of radius a contains a DNA chain segment (surrounded by counter-ions) with backbone inter-charge spacing $\Delta = 0.17$ nm immersed in a binary electrolyte of a specific Debye length. The scale separation among these three length scales, which may give rise to different electric double layer (EDL) approximations, is depicted in Fig. 1. For $\kappa^{-1} \approx 10$ nm (assuming an average ionic concentration), we have a thick EDL within the bead ($\Delta\kappa \ll 1$), which justifies the use of Manning's single particle mobility [13, 18]

$$\mu_0 = \left[\frac{3\pi\eta l_s}{\ln(\Delta/\lambda_D)} + \frac{l_s}{6\lambda_B} \left(\frac{1}{\mu^+} + \frac{1}{\mu^-} \right) \right]^{-1}, \tag{12}$$

where l_s is the contour length of the bead-contained chain segment, $\lambda_B = 0.7$ nm the Bjerrum length of water and $\mu^{\pm}$ the cation and anion mobilities. With 48,502 base pairs (backbone charges) in the λ-phage DNA and $N_s = 10$, we have $l_s = 0.75\,\mu$m. Assuming a 400 mM Tris-Acetate solution as a prototypical electrolyte buffer at 25 °C, we convert the limiting molar ionic conductivities [23] to generalized mobilities and upon substituting into Eq. 12, we obtain $\hat{\mu}_0 = \zeta\mu_0 = 0.67$. The wall contribution $\boldsymbol{\Omega}^{W,e}$ is computed numerically by the same procedure as $\boldsymbol{\Omega}^W$.

Given the rapid decay of the corrections $\boldsymbol{\Omega}^W$ and $\boldsymbol{\Omega}^{W,e}$ in a channel [7], we precompute them with the axial cut-off equal to two times the channel height H. For specific field point and source point locations, $(\boldsymbol{x}_{FP}, \boldsymbol{x}_{SP})$,

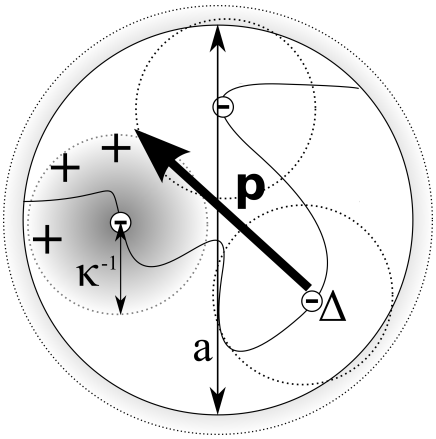

Fig. 1: Separation of length scales: bead radius a, inter-charge spacing Δ and Debye length κ^{-1}. The electrostatic blob of radius κ^{-1} contains weakly interacting chain segment with approximately Gaussian statistics. The effective charge of the blob leads to electrostatic inter-blob repulsion and chain swelling. The backbone charges are partially screened by the counter-ion cloud resulting in an effective dipole moment $\boldsymbol{p}$.

we then perform a set of tri-linear interpolations with the precomputed grid values. Denoting the interpolation operator for a dyad $\boldsymbol{G}(\boldsymbol{x}_{FP}, \boldsymbol{x}_{SP})$ and interpolation nodes $\boldsymbol{x}$ as $L[\boldsymbol{G}; \boldsymbol{x}]$, we have

$$\begin{aligned} \boldsymbol{G}(\boldsymbol{x}_i, \boldsymbol{x}_{SP}) &= L[\boldsymbol{G}(\boldsymbol{x}_i, \boldsymbol{x}_j); \boldsymbol{x}_j] \qquad \text{for } j = 1, 2, \ldots n, \\ \boldsymbol{G}(\boldsymbol{x}_{FP}, \boldsymbol{x}_{SP}) &= L[\boldsymbol{G}(\boldsymbol{x}_i, \boldsymbol{x}_{SP}); \boldsymbol{x}_i] \qquad \text{for } i = 1, 2, \ldots m, \end{aligned} \tag{13}$$

where m and n are the numbers of nearest grid neighbors of the field point and source point, respectively.

The stochastic tensor $\boldsymbol{B}$ in Eq. 8 is computed by Cholesky decomposition, which requires a symmetric and positive-semidefinite $\boldsymbol{D}$ (this requirement is primarily dictated by the fact that $\boldsymbol{D}$ is in effect a covariance matrix). The use of the approximate RPY Green's function $\boldsymbol{\Omega}^{OB}$ results, however, in nonsymmetric $\boldsymbol{D}$ (the reciprocity relation $\boldsymbol{\Omega}_{ij} = \boldsymbol{\Omega}_{ij}^T$ is violated). Only its symmetric part (or, more precisely, the symmetric part of $\boldsymbol{\Omega}^W$, since the free-space contribution is symmetric and divergence-free) is thus used in the decomposition and in the BD equation 8 itself. The analysis of error due to neglect of the anti-symmetric part of $\boldsymbol{\Omega}^W$ and its divergence is presented in Sec. 4.

3 Electric field and imposed flow

Using length scale L equal to channel height H, diffusive time scale $\tau_0 = L^2/(k_bT)$ and thermal force scale $F_0 = k_bT/L$, the Brownian dynamics equation 8 can be non-dimensionalized, with the derived scales for the diffusion and HI tensors $D_0 = k_bT/\zeta$ and $\Omega_0 = \zeta^{-1}$, respectively. With the axially acting electric field $\boldsymbol{F}^e = F^e\boldsymbol{e}_x$, we can then write $\boldsymbol{D}^e \cdot \boldsymbol{F}^e = \boldsymbol{D}^e \cdot Pe_H\boldsymbol{e}_x$, where the Peclet number $Pe_H = \frac{F^eH}{k_bT}$ represents the strength of the electric field (for $L = a$, $Pe_H = Pe$ used in our previous work [9]).

The imposed flow field is a three-dimensional pressure-driven flow. The separation-of-variables solution [24] for a rectangular channel, adapted to our coordinate system and nondimensionalized as above yields the axial velocity

$$\begin{aligned} v_x(y,z) &= 4v_{max}\left[y - y^2 - 8S\right], \\ S &= \sum_{n=0}^{\infty} \frac{(-1)^n \cosh[q(z-1/2)]\cos[q(y-1/2)]}{q^3\cosh[q/2]}, \end{aligned} \tag{14}$$

where $q = (2n+1)\pi$. The maximum velocity v_{max} can be expressed in terms of mean shear rate β_m, which in turn can be related to the Weissenberg number of the bead-spring model, Wi, that we employed in our kinetic theory developments [9]. Denoting

$$v_{max} = \frac{\beta_m\tau_0}{2}, \tag{15}$$

where $\beta_m = Wi_Q/\lambda_Q$, the FENE time scale $\lambda_Q = \zeta q_0^2/(12k_bT)$ and the FENE Weissenberg number $Wi_Q = \sqrt{\frac{q_0}{2b_k}}Wi$, we obtain

$$\beta_m = 6D_0\sqrt{\frac{2q_0^3}{b_k}}Wi, \tag{16}$$

which allows us to represent the strength of the flow field in terms of the Weissenberg number.

Using a remainder estimate for the integral convergence test, we estimate the number of terms N to retain in Eq. 14 from the required tolerance ϵ, $\epsilon = \int_N^\infty \frac{1}{[(2x+1)\pi]^3}dx = \frac{1}{4(1+2N)^2\pi^3}$.

4 On the divergence of the diffusion tensor

Our implementation of the divergence term in Eq. 8 follows Fixman's midpoint method [26], which uses a forward finite difference formula with the

step sizes based on the scaled Wiener increments $\Delta \boldsymbol{w}$; specifically, we have

$$\left(\frac{\partial}{\partial \boldsymbol{r}} \cdot \boldsymbol{D}\right) dt = \frac{\sqrt{2}}{2} \left[\boldsymbol{D}(\boldsymbol{r}^*) - \boldsymbol{D}(\boldsymbol{r})\right] \left[\boldsymbol{B}^{-1}(\boldsymbol{r})\right]^T \cdot \Delta \boldsymbol{w}, \tag{17}$$

where $\boldsymbol{r}^* = \boldsymbol{r} + \sqrt{2}\boldsymbol{B}(\boldsymbol{r}) \cdot \Delta \boldsymbol{w}$. While such an approximation is exact for vanishingly small time steps and convenient to use in Brownian dynamics, the following analysis of the symmetric and anti-symmetric divergence vector fields uses as the step size a uniform grid spacing, which should provide quantitative insight to determine whether the anti-symmetric part is negligible and understanding on the contribution to the migration mechanism.

The divergence of the dyad $\boldsymbol{D}_{ij}$ is computed as follows:

$$\frac{\partial}{\partial \mathbf{r}_j} \cdot \boldsymbol{D}_{ij} = \sum_{j=1}^{N} \sum_{k=1}^{3} \left\{ \sum_{l=1}^{3} \frac{\partial}{\partial x_l} D_{ijkl} \right\} \mathbf{e}_k, \tag{18}$$

where N is the number of beads and the summation convention is invoked on the left hand side. The divergence is evaluated on a uniform 3D grid of dimensions $L \times H \times W$ using a forward difference formula

$$\frac{\partial}{\partial x_l}(D_{ij})_{kl} \approx \frac{D_{kl}(\mathbf{r}_i, \mathbf{r}_j + \Delta \mathbf{r}_j \odot \mathbf{e}_l) - D_{kl}(\mathbf{r}_i, \mathbf{r}_j)}{||\Delta \mathbf{r}_j \odot \mathbf{e}_l||}, \tag{19}$$

where $\Delta \mathbf{r}_j$ is a constant vector of grid spacings, $(\Delta x, \Delta y, \Delta z)$, and the symbol $\odot$ stands for component-wise multiplication. This can be contrasted with Fixman's method where $\Delta \mathbf{r} := \sqrt{2}\boldsymbol{B}(\mathbf{r})\Delta \boldsymbol{w}$. Since $\boldsymbol{D}$ is equal to the HI tensor $\boldsymbol{\Omega}$ up to an isotropic contribution, the divergences of both tensors are identical. After decomposing $\boldsymbol{\Omega}$ into a superposition of the free space $\boldsymbol{\Omega}^{OB}$ and wall contributions $\boldsymbol{\Omega}^{W}$, we note that $\boldsymbol{\Omega}^{OB}$ yields zero divergence for both the Oseen-Burgers (O-B) and Rotne-Prager-Yamakawa tensor (R-P-Y). Thus in the following computations we will work only with $\boldsymbol{\Omega}^{W}$, and more specifically, with its symmetric part, as it is the symmetrized diffusion tensor that is used in Eq. 8.

Without loss of generality, we focus on a pair of beads on the chain and compute the divergence of the diffusion tensor as per Eq. 18 on a finite difference grid in an axially truncated domain described in Sec. 2. We observe how the divergence (vector field), and its magnitude (scalar field), vary with the location of the source point, which is confined to the central cross-section (yz plane) of the channel. We use a central difference formula in the interior of the domain and one-sided formulas at the boundaries.

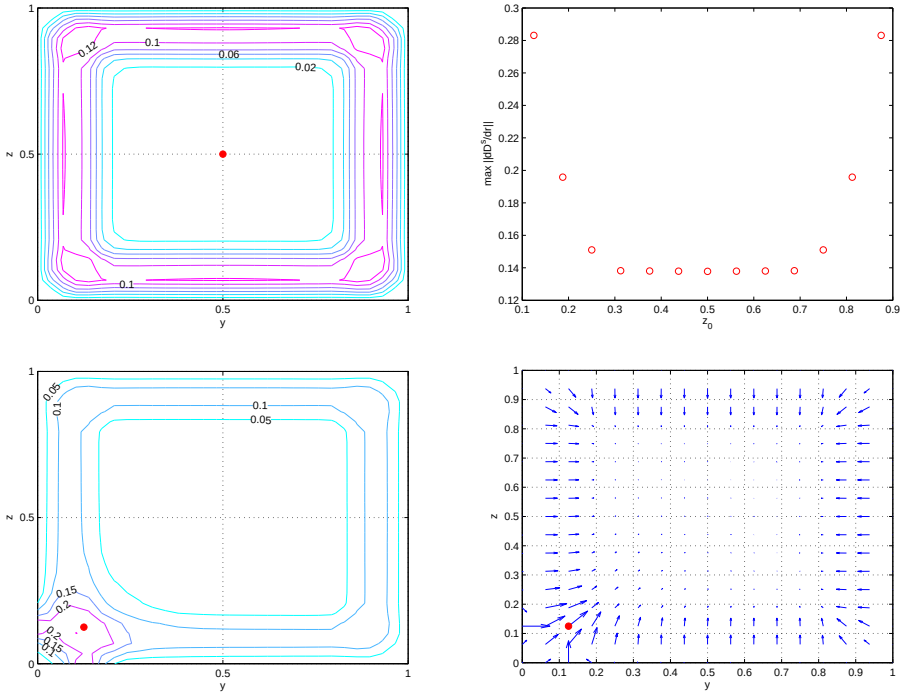

Fig. 2: Upper left: Contours of $\left|\left|\frac{\partial}{\partial \boldsymbol{r}} \cdot \boldsymbol{D}\right|\right|$ for the source point (thick dot) at center of the channel cross-section. Upper right: max $\left|\left|\frac{\partial}{\partial \boldsymbol{r}} \cdot \boldsymbol{D}\right|\right|$ vs z_0, with source point coordinates $\boldsymbol{r}_0 = [x_0, 1/2, z_0]$. Bottom: The divergence field (right) and its contours (left) for the source point near a corner. Diffusivity scaled by $D_0 = k_b T/\zeta$, length by channel height $H = 10\,\mu$m.

Fig. 2 shows that the magnitude of the divergence field exhibits a symmetric (with respect to C_4 rotation) maximum near the walls for a source point located in the center. Asymmetric maxima, also near the walls, arise due to source points located near walls or corners. As the distance z_0 of the source point from the wall increases, the value of the near-wall maximum decreases, reaching minimum for source points located more than $H/3$ from the nearest wall.

The vector field itself shows a consistent contribution to the migration away from the walls irrespective of the location of the source point, which is in agreement with the analytical results that we now briefly summarize. Specifically, the derivation of the free-space regularized RPY tensor (which is based on the assumption of the point force being uniformly distributed over a spherical surface) can be extended to a near-plane case; we can then

express the wall correction $\mathbf{\Omega}^W$ for the RPY tensor in terms of the wall corrections due to a point force, $\mathbf{\Omega}^{W,PF}$ [5]), and due to a potential dipole, $\mathbf{\Omega}^{W,PD}$, yielding [8]

$$\mathbf{\Omega}^W_{ij} = \mathbf{\Omega}^{W,PF}_{ij} - \frac{2a^2}{3}\mathbf{\Omega}^{W,PD}_{ij}. \tag{20}$$

All higher-order singularities of the Stokes flow can be written in terms of the derivatives of the Green's functions. So also can a potential dipole be written in terms of the Laplacian of the point-force solution, $\mathbf{\Omega}^{W,PD}_{ij} = -\frac{1}{2}\nabla_i^2\mathbf{\Omega}^{W,PF}$, where ∇_i indicates derivatives with respect to $\boldsymbol{r}_i$. This reduces the problem of finding the wall correction due to the potential dipole to differentiating a well-established solution due to Blake [5]. However, since the addition of the potential dipole ruins the reciprocity relation, it is a common practice [12, 8] to symmetrize $\mathbf{\Omega}^{W,PD}$, finally arriving at

$$\mathbf{\Omega}^W_{ij} = \left[1 + \frac{a^2}{6}\left(\nabla_i^2 + \nabla_j^2\right)\right]\mathbf{\Omega}^{W,PF}_{ij}. \tag{21}$$

Assuming the wall is in the z-direction, the diffusivity tensor divergence of the i-th bead can than be evaluated according to Eq. 18, leading to the only non-zero term being that due to self-diffusivity ($i = j$), in the form (cf. [8])

$$\left[\frac{\partial}{\partial\hat{\boldsymbol{r}}}\cdot\hat{\boldsymbol{D}}\right]_i = \left(\frac{9}{8\hat{z}_i^2} - \frac{3}{2\hat{z}_i^4}\right)\boldsymbol{e}_z, \tag{22}$$

where $\boldsymbol{e}_z$ is the unit vector in the z-direction and we scaled the diffusivity and length by D_0 and a, respectively. The bracketed prefactor is positive for $\hat{z} \geq 1.16$, leading to migration away from the walls, in agreement with our numerical results for a square channel.

As the anti-symmetric part of the wall correction due to the potential dipole is effectively neglected from both the diffusion tensor $\boldsymbol{D}$ and its divergence, we quantify the resulting error by computing spatial decay of the non-zero components of the relevant dyad for a bead in contact with wall (which yields the largest error). Fig. 3 shows that only the velocity normal to the wall will be affected by the error and confirms rapid decay of the error as the field point moves away from the source point in both tangential and normal directions with respect to the wall. The divergence of the anti-symmetric part is identically zero.

Using the method described, we also computed the divergence of the electrophoretic mobility tensor, $\frac{\partial}{\partial\boldsymbol{r}}\cdot\boldsymbol{\mu}^e = \frac{\partial}{\partial\boldsymbol{r}}\cdot\mathbf{\Omega}^{W,e}$. The qualitative picture is similar to Fig. 2, with the magnitudes of the divergence field proportional

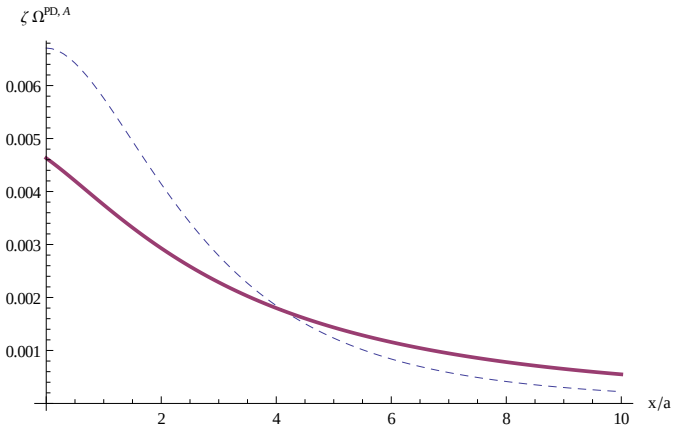

Fig. 3: The decays of the anti-symmetric part of the wall correction dyad due to a potential dipole. Source point touching the wall, with unit wall normal $\boldsymbol{e}_z$. Solid line: (z,z) component as the field point moves away from the source point in wall-normal direction. Dashed line: (z,x) and (z,y) components as the field point moves away from the source point in wall-tangential directions, x and y.

to κ: in the limit of $\kappa \to 0$, we have $\boldsymbol{\Omega}^{LA} = \boldsymbol{\Omega}^{OB}$ with the dependences identical to those in Fig. 2. As κ increases, the Debye length decreases and so does the magnitude of the electrophoretic diffusion tensor $\boldsymbol{D}^e$; the increased screening of electrostatic interactions thus results in a negligible influence of the external force on the chain configuration.

5 Cross-stream migration

While cross-stream migration mechanisms have been explained in terms of the kinetic theory of dumbells near planar walls ([12, 17, 13]), the proposed explanations may not be always satisfactory or applicable. We now review the theory and relate the observed phenomena to the center-of-mass flux, whose steady-state wall-normal component predicts the migration patterns. The predictions are qualitatively consistent with the results of Brownian dynamics simulations presented in Sec. 6 and facilitate their interpretation.

The migration part of the flux, $[\boldsymbol{j}_C]_{mig}$, contains the superposition of four migration (drift, convection) terms, given by [13, 17]

$$[\boldsymbol{j}_C]_{mig} = n\left[\frac{1}{2}\langle\bar{\boldsymbol{\Omega}}\cdot\boldsymbol{F}^s\rangle + \frac{2}{k_bT}\langle\boldsymbol{D}_{\boldsymbol{K}}\cdot\boldsymbol{F}^e\rangle - \frac{\partial}{\partial\boldsymbol{r}_c}\cdot\langle\boldsymbol{D}_{\boldsymbol{K}}\rangle + \frac{k_bT}{2}\langle\bar{\boldsymbol{\Omega}}\cdot\frac{\partial}{\partial\mathbf{Q}}\ln\psi\rangle\right], \tag{23}$$

where $\boldsymbol{D_K}$ and $\bar{\boldsymbol{\Omega}}$ are linear functions of the HI tensor $\boldsymbol{\Omega}_{ij}$ and n and ψ are the center-of-mass and bond vector distribution functions, respectively. The competition among these terms predicts the overall migration direction, i.e. away from the wall (AFW) or towards the wall. The linear functions of the HI tensor $\boldsymbol{\Omega}$ are defined as [17]

$$\begin{aligned}\bar{\boldsymbol{\Omega}} &= (\boldsymbol{\Omega}_{11} - \boldsymbol{\Omega}_{22}) + (\boldsymbol{\Omega}_{21} - \boldsymbol{\Omega}_{12}) \\ \bar{\bar{\boldsymbol{\Omega}}} &= (\boldsymbol{\Omega}_{11} - \boldsymbol{\Omega}_{22}) + (\boldsymbol{\Omega}_{12} - \boldsymbol{\Omega}_{21}) \\ \boldsymbol{D_K} &= \frac{1}{4}(\boldsymbol{D}_{11} + \boldsymbol{D}_{22} + \boldsymbol{D}_{21} + \boldsymbol{D}_{12}),\end{aligned} \tag{24}$$

where $\boldsymbol{\Omega}_{ii}$ represent bead mobilities, $\boldsymbol{\Omega}_{ij}$ represent the inter-bead HI interactions and $\boldsymbol{D_K}$ is the Kirkwood diffusivity averaged over the internal coordinates.

5.1 Internally-induced HIs (IHIs due to $\boldsymbol{F}^S$)

We note that the dominant term in shear flows is the deterministic term proportional to internal spring tension $\langle \bar{\boldsymbol{\Omega}} \cdot \boldsymbol{F}^S \rangle$, where the angle brackets denote an ensemble average with respect to the distribution function ψ (this terms is directly proportional to the stress tensor $\boldsymbol{\tau}_P$[17]). The average dumbell orientation is 45 degrees with respect to the wall, induced by the flow. For dumbells parallel and perpendicular to the walls the migration is AFW and towards the wall, respectively. As $\bar{\boldsymbol{\Omega}} = 0$ in bulk, this is a wall-mediated hydrodynamic interaction (WHI), whose strength increases with the spring force $\boldsymbol{F}^S$, i.e. indirectly with effective shear rate, which dictates the amount of average stretch of the chain.

5.2 Externally-induced HIs (EHIs due to $\boldsymbol{F}^E$)

The term proportional to the external (e.g. electric) force, $\langle \boldsymbol{D_K} \cdot \boldsymbol{F}^E \rangle$, is dominant in electrophoresis. The average dumbell orientation is again 45 degrees with respect to the wall, however induced by WHI (due to the term $\bar{\bar{\boldsymbol{\Omega}}} \cdot \boldsymbol{F}^E$ appearing in the equation of motion for $\boldsymbol{Q}$ [10] rather than the flow. The direction of migration will be determined primarily by the magnitude and direction of the electric force.

As $\bar{\bar{\boldsymbol{\Omega}}} = 0$ in bulk, but $\boldsymbol{D_K} \neq 0$, we have an interesting coupling effect in bulk: a superimposed flow (e.g. shear) provides the required orientation of the dumbell for the migration to take place. Without the flow, however, the orientation is uniformly distributed and $\langle \boldsymbol{D_K} \cdot \boldsymbol{F}^E \rangle$ averages to zero, yielding no net migration. This coupling is represented in the theory by the term

proportional to the product of Wi and Pe. The main conceptual difference from the internally-induced HIs is that here the net migration force on the center-of-mass does not average to zero.

5.3 Diffusion-induced HIs (DHIs due to $\boldsymbol{F}^B$)

The term proportional to the Brownian force, $-\frac{\partial}{\partial \boldsymbol{r}_c} \cdot \langle \boldsymbol{D}_{\boldsymbol{K}} \rangle$, is important only in the case of a nonuniform velocity gradient (e.g. Poiseuille flow). While the divergence of the diffusion tensor leads to migration AFW (as we showed in Eq. 22 in the context of Brownian dynamics), the negative sign gives rise to migration away from the centerline (where this term is dominant as the internally-induced HIs vanish by symmetry). We call these primary diffusion-induced HIs.

An additional Brownian drift term, proportional to $\langle \bar{\boldsymbol{\Omega}} \cdot \frac{\partial}{\partial \mathbf{Q}} \ln \psi \rangle$ (or, alternatively, $\frac{\partial}{\partial \boldsymbol{r}_1} \cdot \boldsymbol{D}_{11} + \frac{\partial}{\partial \boldsymbol{r}_2} \cdot \boldsymbol{D}_{22}$ [12]), leads to weak migration AFW, according to Eq. 22. This term vanishes in the kinetic theory after linearization of $\bar{\boldsymbol{\Omega}}$. We call these secondary diffusion-induced HIs.

Note that both internally and externally induced HIs are deterministic in nature, as opposed to DHIs which are driven by Brownian force. Unlike bulk HIs, wall-mediated HIs are crucial in capturing cross-migration, as demonstrated by the Brownian dynamics simulations [12]. Table 1 summarizes the migration phenomena observed with commonly used models. For the free draining model, $\bar{\boldsymbol{\Omega}} = 0$ and $\boldsymbol{D} = \boldsymbol{I}$, yielding no IHIs and no DHIs and thus no migration. For the bulk HI model, where we have $\boldsymbol{D} = \boldsymbol{I} + \boldsymbol{\Omega}^{OB}$, $\bar{\boldsymbol{\Omega}}$ remains zero. We thus have IHIs and secondary DHIs still absent, but the primary DHIs are now non-zero. For the reduced model, where we prioritize WHI at the expense of bulk HI, i.e. $\boldsymbol{D} = \boldsymbol{I} + \boldsymbol{\Omega}^{W}$, $\bar{\boldsymbol{\Omega}}$ is no longer zero; in fact, $\bar{\boldsymbol{\Omega}} = \boldsymbol{\Omega}_{11} - \boldsymbol{\Omega}_{22}$. DHIs are thus fully present while IHIs are weakened due to the incomplete $\bar{\boldsymbol{\Omega}}$. The full HI model, with the complete and dominant IHIs accurately predicts the migration AFW.

The limitations of the kinetic theory include the failure of the dumbell model in fast flows due to insufficient number of relaxation modes and the failure of the linearization of the Green's function for chains stretched beyond the distance of the center-of-mass from the nearest wall. With the above classificiation of HIs we now return to the Brownian dynamics of dilute polymer solutions.

Table 1: The effect of bulk HIs and WHIs in BD simulations on cross-stream migration. 0 and 1 in the second column denote exclusion and inclusion of the relevant HI terms, respectively. No external force present.

Model name	[HI, WHI]	observed migration
Full HIs	[1,1]	full
Reduced model	[0,1]	reduced
Bulk HIs	[1,0]	opposite
Free draining	[0,0]	none

5.4 Hydrodynamic interactions in competition

In weak confinement (channel height $H = O(100R_g)$), Kekre [13] observes migration only in combined electrophoresis and Poiseuille flow, not when the fields are applied individually. This is in agreement with the coupling effect observed in bulk (discussed in Sec. 5.2), as the wide wall separation used here mimics the bulk behavior. They further observe in the combined flow a minimum in the concentration layer thickness w (defined as the width of the region that contains 95% of the polymer concentration) versus Pe (or Wi^E), which follows the minimum in the magnitude of the radius of gyration tensor. However, it should be pointed out that the real source of the nonmonotonic behavior is the competition between EHIs (dominant near walls) and DHIs (dominant near centerline); we can thus expect saturation at high Pe. Similar competition can be seen for the dependence of w on channel height H, as observed by Jendrejack [12]. Their explanation of the individual regions of the dependence curve appears, however, rather controversial: as the channel width increases, the strength of the pressure-driven flow must decrease (contrary to what is suggested); also, we assume that increased sampling of the near-wall region due to increased chain stretch would only be relevant for the static depletion layer, not the non-equilibrium one being studied. In addition, HI depletion effects become unimportant as H increases, not the other way around as proposed.

To provide a more systematic explanation for the non-monotonic dependence of w on H with the maximum for small H observed in [12], it is convenient to decouple the two superimposed effects of deterministic and Brownian (random) HIs. The former results in monotonic increase in w with increasing H. This is because the inner core of the fluid, where WHIs are negligible, expands proportionally to the wall separation distance, at the expense of the boundary layer where WHIs are dominant. We can ex-

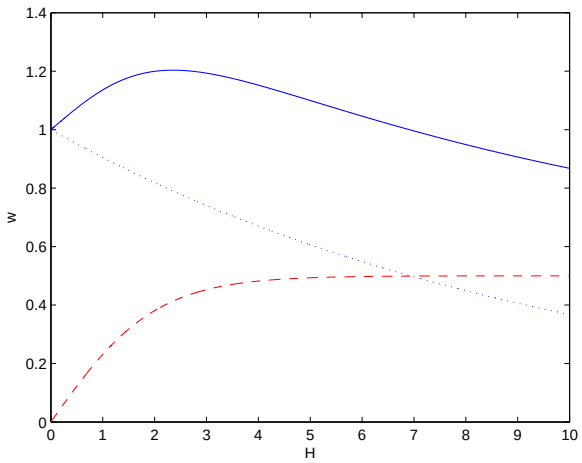

Fig. 4: A qualitative model of the competition between deterministic HIs (dashed) and Brownian HIs (dotted), yielding the observed dependence upon superposition (solid). Note the saturation at large H for deterministic HIs. w normalized by its equilibrium value, units of H are arbitrary.

pect saturation at large H as the WHIs will have decayed below a negligible tolerance. The impact of the latter, Brownian DHIs, on w can be gleaned from particle suspension studies in pressure-driven flow [19]. These confirm flattening of the velocity profile as H increases, with the corresponding decrease in mean shear rate and diffusivity. The flow thus becomes more homogeneous, and we can expect the divergence of the diffusion tensor to also decrease with increasing H. The contribution of DHIs to w vs H will thus have a decreasing character. To give a qualitative picture, we plot the contributions due to deterministic and Brownian HIs as a logistic function and decaying exponential, respectively, revealing the non-monotonic dependence upon superposition of the two, Fig. 4.

6 Simulation results

The Brownian dynamics implementation described in Sec. 2, with wall corrections due to both the regular Oseen-Burgers and the electrophoretic Long-Ajdari HI tensors, is followed for the period of 10 Rouse relaxation times with a time step $\Delta t = 10^{-3}$ (nondimensionalized by a^2/D_0). At the initial time, 11-bead chains in zig-zag conformation are uniformly distributed throughout a rectangular domain with grid spacing approximately 4 beads per grid

cell and the axial cut-off of wall-mediated HIs and electrically-induced HIs equal to $2H$ (taking advantage of the mirror symmetry with respect to the central cross-section, only half-domain is retained after pre-computation and pre-interpolation of the HI tensors for computational efficiency). To model moderate confinement, we choose channel height $H = 10\,\mu$m. Multiple realizations, each with a randomly seeded sequence of pseudo-random Wiener increments, were performed and averaged. The concentration profiles are constructed using a Gaussian-kernel density estimator with the bandwidth set so as to obtain smooth profiles while retaining all statistically significant features.

The migration patterns we observe in the simulations are consistent with the theoretical predictions. In the absence of an electric field ($Pe = 0$), Fig. 5 demonstrates increased migration towards the centerline with increasing Wi. The migration is purely shear-induced (IHIs) and being wall-mediated, it is not observed in weak confinements. The degree of migration can be quantified by the concentration layer thickness w, defined as the second moment of the center-of-mass probability density. Correspondingly, as Wi increases, we observe a decrease in the concentration layer thickness.

As our focus is the competition between migration towards and away from the walls, we study the combined Poiseuille flow and electric field acting in mutual opposition, with Debye length $\lambda_D = 1\,\mu$m (low electrolyte concentration, minimal screening of electrically induced HIs). Fig. 6 shows the effect of increasing Wi with moderate electric field strength ($Pe = 20$). While for $Wi = 10$ a bimodal distribution with two polymer concentration maxima near the walls develops, with increasing Wi the migration towards the walls is gradually suppressed at the expense of the migration towards the centerline, with the latter dominating for large enough Wi. Fig. 7 shows the effect of increasing Pe under moderate flow conditions ($Wi = 10$). A similar trend is observed: for large Pe, the competition is strongly in favor of the migration towards the centerline. Fig. 5, 6 and 7 also show the transition between the two migration regimes under increasing electric field strength. For moderate flow strength, we see the nonmonotonic dependence of the maximum of the concentration profile on Pe, as the maximum is shifted towards the walls, and back to the center, for moderate and high Pe, respectively.

As λ_D decreases, the electrostatic screening of electrically-induced HIs becomes prominent. As shown in Fig. 8, the migration effects are strongly suppressed when the Debye length is reduced to $\lambda_D = 140$ nm. While weak migration towards the wall persists, it is no longer opposed by migration AFW at large Pe. This is further demonstrated in Fig. 9 by the concentra-

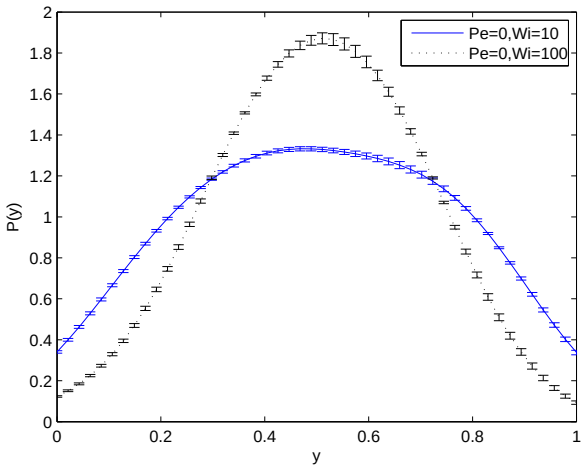

Fig. 5: The center-of-mass probability density for non-zero Wi, with $Pe = 0$. As Wi increases from 10 to 100, the concentration layer thickness w/w_{eq} decreases from 0.87 to 0.55, where w_{eq} is the equilibrium value which corresponds to uniform distribution.

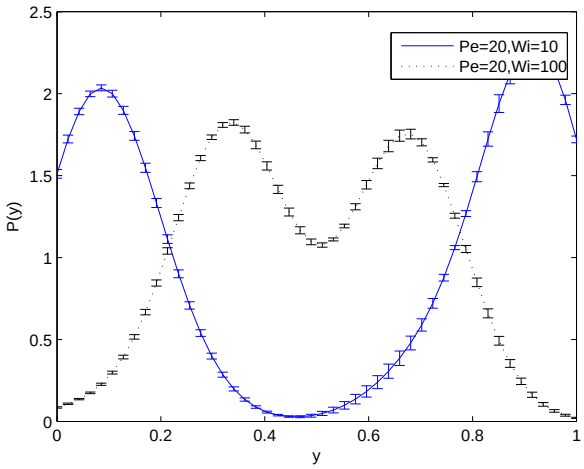

Fig. 6: The center-of-mass probability density for varying Wi and fixed Pe, with the flow field and electric field in opposition. The competition between migration towards, and away from, the wall is evident.

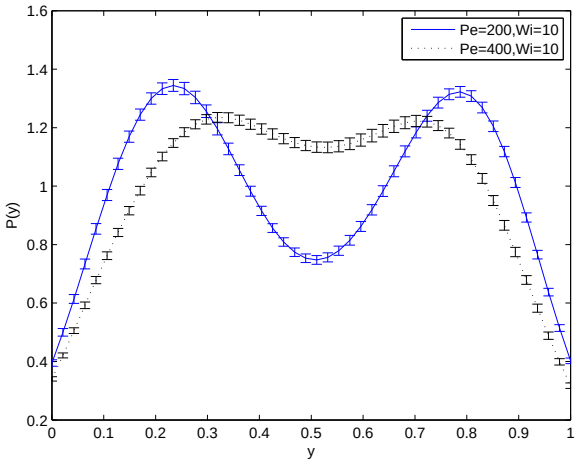

Fig. 7: The center-of-mass probability density for varying Pe and fixed Wi, with the flow field and electric field in opposition.

tion layer thickness monotonically increasing with the Peclet number and gradually saturating. In the limit of $\lambda_D \to 0$, the electrophoretic wall correction $\mathbf{\Omega}^{W,e}$ vanishes, as does the corresponding mobility tensor $\boldsymbol{\mu}^e$. In the other limit of $\lambda_D \to \infty$, we recover the regular Stokeslet hydrodynamics, i.e. $\mathbf{\Omega}^{W,e} = \mathbf{\Omega}^{W}$.

We conclude that computational models, or equivalently theoretical predictions of the kinetic theory, that do not include the wall correction $\mathbf{\Omega}^{W,e}$ to the electrophoretic Stokeslet in the mobility tensor $\boldsymbol{\mu}^e$ (Eq. 6) will underestimate the effects of migration. On the other hand, given the slower decay of a regular Stokeslet (and its wall correction) compared to that of an electrophoretic Stokeslet, we may infer that models that replace the wall correction $\mathbf{\Omega}^{W,e}$ due to the Long-Ajdari Stokeslet by the wall correction $\mathbf{\Omega}^{W}$ due to regular Oseen-Burgers Stokeslet will over-estimate the influence of electrically-induced HIs. The error of such approximation is proportional to κ and vanishes for $\kappa \to 0$.

Next, we compare the results between the simulations with and without the electrophoretic wall correction. To examine the migration for Poiseuille flow and electric field in opposition in more detail, we plot the dependence of the concentration layer thickness on the Peclet number for moderate flow strength ($Wi = 10$) in Fig. 10. We again observe migration towards and away from the walls for small and large electric field strengths, respectively, as consistent with Fig. 5-7. However, when the wall correction is neglected,

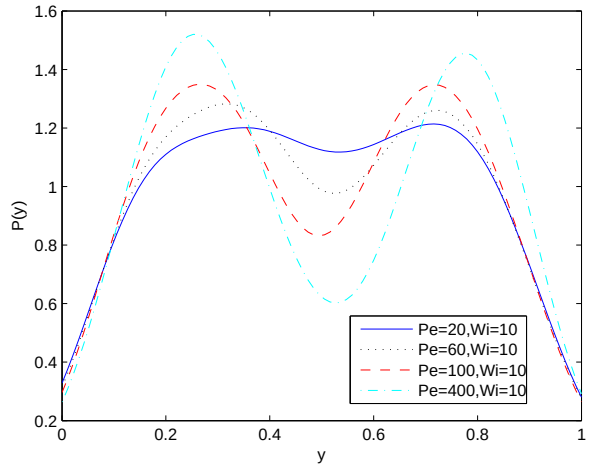

Fig. 8: The center-of-mass probability density for varying Pe and fixed Wi, with the flow field and electric field in opposition and Debye length decreased to $\lambda_D = 140$ nm.

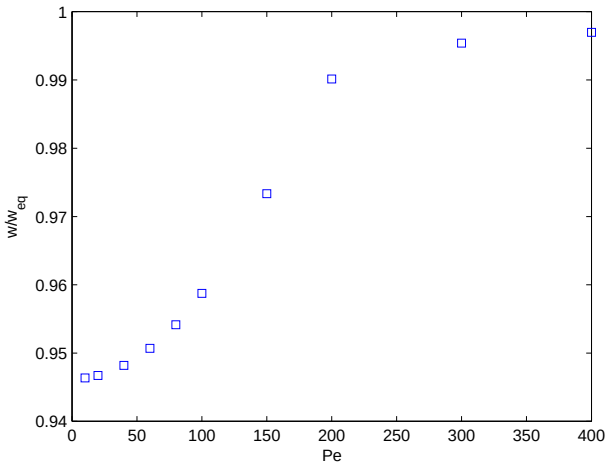

Fig. 9: Concentration layer thickness, scaled by w_{eq} versus electric field strength for $Wi = 10$ and Debye length decreased to $\lambda_D = 140$ nm.

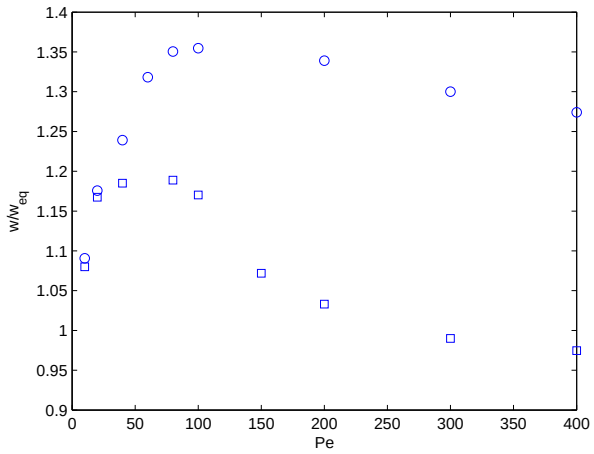

Fig. 10: Concentration layer thickness, scaled by w_{eq} versus electric field strength for $Wi = 10$. Transition from the migration towards the walls to the migration towards the centerline is evident. Electrophoretic correction: $\bigcirc$ = excluded; $\square$ = included.

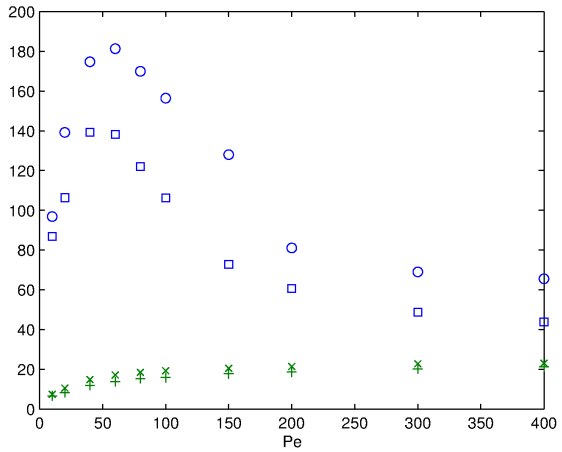

Fig. 11: Shape descriptors ($\bigcirc, \square$ = chain asphericity S_{xx}/S_{yy} and $\times, +$ = the trace of the gyration tensor $Tr(S)$), scaled by q_0^2, versus electric field strength for $Wi = 10$. Transition between chain extension and compression in the axial direction as Pe increases. Electrophoretic correction: $\bigcirc, \times$ = excluded; $\square, +$ = included.

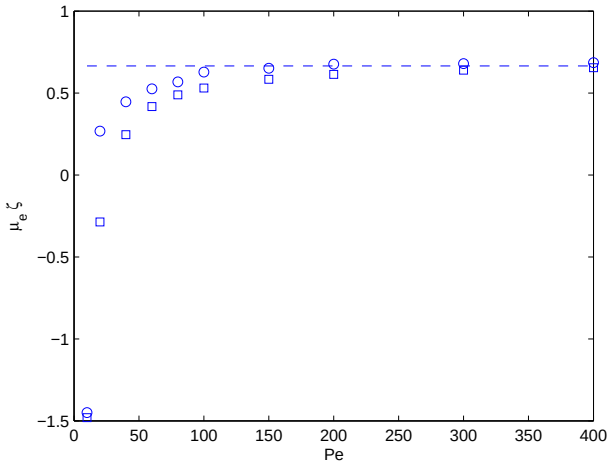

Fig. 12: Electrophoretic mobility μ_e, scaled by ζ, versus electric field strength for $Wi = 10$. Flow reversal occurs at $Pe_r \approx 50$, saturation occurs at Manning's mobility $\mu_0\zeta = 0.67$. Electrophoretic correction: ○ = excluded; □ = included.

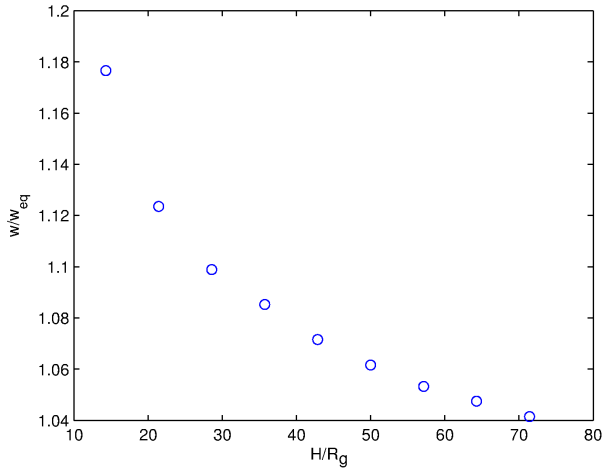

Fig. 13: Concentration layer thickness (scaled by w_{eq}) versus channel height (scaled by radius of gyration). A monotonic decrease characteristic of moderate and weak confinements. $Wi = 10$, $Pe = 20$.

the absence of an important contribution to the migration AFW is immediately reflected in the overprediction of migration towards the wall at small Pe and underprediction of migration AFW at large Pe. As demonstrated in Fig. 11, the dependence of w closely follows that of the asphericity of the chain in the axial direction, defined as S_{xx}/S_{yy}, where $\boldsymbol{S}$ is the gyration tensor. As the chain migrates towards the walls, the shear rate increases and so does the axial chain extension. For large Pe, the chain experiences axial compression in the region with small shear rate near the centerline. Again, the effects are under-estimated when the electrophoretic wall correction is neglected. The overall chain size, quantified by the trace of the gyration tensor $Tr(\boldsymbol{S})$, shows a slow and monotonic increase with Pe. Similarly, the electrophoretic mobility μ_e, depicted in Fig. 12, increases steadily with the electric field strength, undergoing a flow reversal ($\mu_E = 0$) and saturating for large Pe at Manning's particle mobility μ_0. This indicates that the wall-mediated HIs become unimportant due to their fast decay as the chain swells and the inter-bead distances increase. The saturation occurs at lower Pe when the wall correction is neglected.

As evidenced in Fig. 10 and 11, when the correction is included, the transition between the migration regimes occurs at $Pe_t \approx 60$, which appears closely related to the flow reversal occurring at $Pe_r \approx 50$ (Fig. 12). This value corresponds to the balance between the Weissenberg and Peclet numbers, which yields $Pe_r = \frac{H}{\sqrt{2b_k q_0^3 \mu_0 \pi \eta}}$.

Fig. 13 shows monotonic decrease of the concentration layer thickness with channel height, as expected for moderate and weak confinements based on the qualitative model in Fig. 4.

References

[1] S.A. Allison and D. Stigter, *A commentary on the screened-Oseen, counterion-condensation formalism of polyion electrophoresis*, Biophysical journal **78** (2000), no. 1, 121–124.

[2] R. Ashton, C. Padala, and R.S. Kane, *Microfluidic separation of DNA*, Current opinion in biotechnology **14** (2003), no. 5, 497–504.

[3] A.A.S. Bhagat, H. Bow, H.W. Hou, S.J. Tan, J. Han, and C.T. Lim, *Microfluidics for cell separation*, Medical and Biological Engineering and Computing **48** (2010), no. 10, 999–1014.

[4] R.B. Bird, R.C. Armstrong, and O. Hassager, *Dynamics of polymeric liquids. Vol. 1: Fluid mechanics*, (1987).

[5] JR Blake, *A note on the image system for a Stokeslet in a no-slip boundary*, Proc. Camb. Phil. Soc, vol. 70, Cambridge Univ Press, 1971, pp. 303–310.

[6] J.E. Butler, O.B. Usta, R. Kekre, and A.J.C. Ladd, *Kinetic theory of a confined polymer driven by an external force and pressure-driven flow*, Physics of Fluids **19** (2007), 113101.

[7] H. Diamant, *Hydrodynamic interaction in confined geometries*, arXiv preprint arXiv:0812.4971 (2008).

[8] N. Hoda and S. Kumar, *Brownian dynamics simulations of polyelectrolyte adsorption in shear flow with hydrodynamic interaction*, The Journal of chemical physics **127** (2007), 234902.

[9] P. Hotmar and R. Chella, *Kinetic theory of a charged FENE dumbell in confined flow under applied pressure and electric fields*, pre-print.

[10] ———, *Voltage-driven polymer translocation through nanopores and entropic traps*, pre-print.

[11] R.M. Jendrejack, J.J. De Pablo, and M.D. Graham, *Stochastic simulations of DNA in flow: Dynamics and the effects of hydrodynamic interactions*, The Journal of chemical physics **116** (2002), 7752.

[12] R.M. Jendrejack, D.C. Schwartz, J.J. De Pablo, and M.D. Graham, *Shear-induced migration in flowing polymer solutions: Simulation of long-chain DNA in microchannels*, The Journal of chemical physics **120** (2004), 2513.

[13] R. Kekre, *Role of hydrodynamic interactions in dynamics of semi-flexible polyelectrolytes*, (2011).

[14] R. Kekre, J.E. Butler, and A.J.C. Ladd, *Role of hydrodynamic interactions in the migration of polyelectrolytes driven by a pressure gradient and an electric field*, Physical Review E **82** (2010), no. 5, 050803.

[15] R.G. Larson, *The rheology of dilute solutions of flexible polymers: Progress and problems*, Journal of rheology **49** (2005), 1.

[16] D. Long and A. Ajdari, *A note on the screening of hydrodynamic interactions, in electrophoresis, and in porous media*, The European Physical Journal E: Soft Matter and Biological Physics **4** (2001), no. 1, 29–32.

[17] H. Ma and M.D. Graham, *Theory of shear-induced migration in dilute polymer solutions near solid boundaries*, Physics of Fluids **17** (2005), 083103.

[18] G.S. Manning, *Limiting laws and counterion condensation in polyelectrolyte solutions. V. Further development of the chemical model*, Biophys. Chem **9** (1978), 65–70.

[19] P.R. Nott and J.F. Brady, *Pressure-driven flow of suspensions: simulation and theory*, Journal of Fluid Mechanics **275** (1994), no. 1, 157–199.

[20] H.C. Öttinger, *Stochastic processes in polymeric fluids: tools and examples for developing simulation algorithms*, Springer Berlin,, New York, 1996.

[21] H.C. Öttinger and Y. Rabin, *Diffusion equation versus coupled Langevin equations approach to hydrodynamics of dilute polymer solutions*, Journal of rheology **33** (1989), no. 5, 725–743.

[22] N.A. Petersson, *Stability of pressure boundary conditions for Stokes and Navier–Stokes equations*, Journal of Computational Physics **172** (2001), no. 1, 40–70.

[23] E. Stellwagen and N.C. Stellwagen, *Probing the electrostatic shielding of DNA with capillary electrophoresis*, Biophysical journal **84** (2003), no. 3, 1855–1866.

[24] G.A. Truskey, F. Yuan, and D.F. Katz, *Transport phenomena in biological systems*, vol. 82, Pearson Prentice Hall Upper Saddle River, NJ, 2004.

[25] L.Y. Yeo, H.C. Chang, P.P.Y. Chan, and J.R. Friend, *Microfluidic devices for bioapplications*, small **7** (2011), no. 1, 12–48.

[26] Y. Zhang, *Brownian dynamics simulation of DNA in complex geometries*, Ph.D. thesis, 2012.

[27] J. Zheng and E.S. Yeung, *Anomalous radial migration of single DNA molecules in capillary electrophoresis*, Analytical chemistry **74** (2002), no. 17, 4536–4547.